Trends and Variability in Airmass Frequencies: Indicators of a Changing Climate

CAMERON C. LEE

Kent State University, Kent, Ohio

(Manuscript received 12 February 2020, in final form 14 July 2020)

ABSTRACT

Recent international efforts at communicating climate change have begun using the notion of a climate indicator—a climate-related metric that can be used to track changes in the Earth system over time. Based upon a recently developed global-scale classification of daily air masses, this research examines the trends and variability in the frequencies of these air masses and then utilizes them to develop two nontraditional climate indicators: a warm/cool index (WCI) and a global extremes index (GEI). Results show that both indices trend significantly upward over the 40-yr period of record, indicating an increase in warm-based air masses (WCI) and extreme air masses (GEI). The two indices also exhibit a moderate (GEI) to strong (WCI) association with the global mean temperature record, multiple near-surface climate variables, and other existing climate indicators over that same time, showing promise as global indicators. Shorter-term variability in these indices also show a linear relationship between the WCI and changes in the Atlantic multidecadal oscillation and a nonlinear relationship between GEI and El Niño–Southern Oscillation. While many published climate indicators are based upon a *single variable*, and/or are regional in scope, the two indices presented herein are unique in that they are representative of the trends in the *multivariate* (and extreme, in the case of the GEI) weather conditions that are experienced near Earth's surface, while also being global in scope.

KEYWORDS: Atmosphere; Climate change; Climatology

1. Introduction

As the planet continues to warm, communicating the reality of our changing climate is becoming ever more important. Recent efforts by the United Nations Framework Convention on Climate Change and multiple agencies in the United States have begun exploring the use of climate indicators as a metric to track the long-term change in our climate system and effectively communicate these changes with the public and policymakers (Williams and Eggleston 2017). According to the U.S. Global Change Research Program (USGCRP), "indicators are observations or calculations that can be used to track conditions and trends. Indicators related to climate—which may be physical, ecological, or societal—can be used to understand how environmental conditions are changing, assess risks and vulnerabilities, and help inform resiliency and planning for climate impacts" (USGCRP 2019). The USGCRP also notes that part of what makes a good indicator is that there is a change over time, there is a clear relationship to a changing climate, and that it is representative of a broad geographic area (USGCRP 2018). To date, a number of indicators have been developed, using traditional climate variables (e.g., heat waves, surface temperatures, heavy precipitation events), extreme events (Alexander et al. 2006), and nontraditional climate and climate-related variables (e.g., length of the frost-free season, heating and cooling degree-days, ocean chlorophyll levels; USGCRP 2019).

In 2014, a new gridded weather typing classification (GWTC) scheme was developed in order to create a spatially cohesive categorization of synoptic-scale weather types (analogous to air masses in the midlatitudes) based upon multivariate surface weather conditions (Lee 2014; Fig. 1). This classification system has recently been expanded to cover a global scale (the GWTC2), use more robust methods for defining air masses (AMs), and—importantly for this research—define more extreme AMs (Lee 2020a). However, the longer-term trends in the frequencies of these multivariate air masses and their shorter-term variability have yet to be examined.

Supplemental information related to this paper is available at the Journals Online website: https://doi.org/10.1175/JCLI-D-20-0094.s1.

Corresponding author: Cameron Lee, cclee@kent.edu

DOI: 10.1175/JCLI-D-20-0094.1

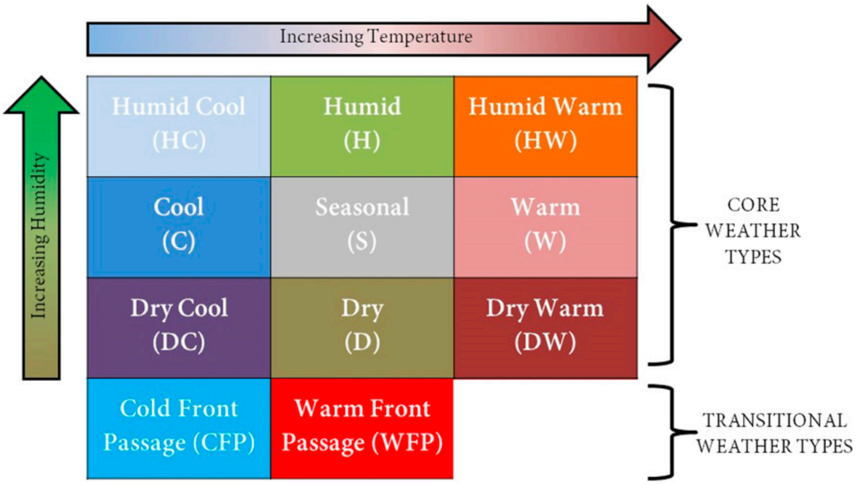

FIG. 1. The structure of the 11 GWTC2 air masses. Modified with permission from http://www.personal.kent.edu/~cclee/gwtc2global.html.

Building upon the aforementioned effort to examine nontraditional indicators of our global climate, the aim of this research is to provide further evidence of the broad scope of the cascading impacts of changes in global mean temperature by 1) investigating airmass trends and variability, 2) outlining the development of two global-scale indices based upon these GWTC2 air masses: a global warm/cool index (WCI) and a global extremes index (GEI), and 3) analyzing their efficacy as indicators of global climate change. These two indicators are simplified answers to the overarching research question: How are the frequencies of air masses changing through time? Since low-frequency internal climate variability—in the form of teleconnections and oscillations (T&O)—plays an important role in modulating the variability of AMs and these two indices (and can mask secular trends), the relationship between AMs, the two GWTC2-based climate indices (GCIs) and T&Os will also be explored.

2. Methods

a. Data: Background and treatment

Daily scale GWTC2 data were retrieved from Lee (2020b) for the entire globe, 1979–2018. In its simplest description, the GWTC2 is a categorization of near-surface weather conditions. Since the weather that impacts our daily lives is both transient and multivariate in nature, the GWTC-2 uses 3-hourly (eight times daily) values of six different deseasonalized near-surface meteorological variables [2-m temperature, 2-m dewpoint, 10-m u and v components of wind, total cloud cover, and sea level pressure (SLP)] in order to classify every day at every location (globally at a 0.5° × 0.5° spatial resolution) into one of 11 different "weather types" or air masses (Fig. 1) that are relative to season and location. There are nine "core" air masses that consist of three partitions each for temperature and humidity (dewpoint), ranging from humid warm to dry cool on one diagonal axis, to humid cool to dry warm on the other. Since many days are characterized more by the *change* in weather than they are by any static conditions, there are also two transitional AMs, which aim to identify conditions associated with cold front passages (CFP) and warm front passages (WFP). All data for this classification were obtained from the Climate Forecast System (CFS; Saha et al. 2010, 2014) of the National Oceanic and Atmospheric Administration of the United States and based upon a 1981–2010 baseline climatology. While a full description of the methodology behind the GWTC2 is beyond the scope of this paper, full details of the GWTC2 can be found in Lee (2020a).

T&O data were collected for the 16 different T&Os listed in Table S4 in the online supplemental material, along with their sources and data treatment. Unless otherwise noted, all data were obtained at monthly resolution for the 1979–2018 period of study. While all 16 T&Os were analyzed in terms of their relationship with the GCIs, many exhibited weak and insignificant correlations with the two GCIs and have thus been omitted from the analysis. In addition, while some statistically significant results emerged from correlative analyses between the GCIs and the Pacific decadal oscillation (PDO), Arctic Oscillation (AO), Antarctic Oscillation (AAO), North Atlantic Oscillation (NAO), east Atlantic (EA), Pacific–North American (PNA), east Atlantic/western Russia (EA/WR) and the tropical

Northern Hemisphere (TNH) T&Os, all were considered fairly weak (absolute value rho < 0.35). While results of these analyses are shown below, for the sake of brevity, an extensive discussion of these T&Os was deemed unwarranted. Thus, the majority of the focus is on two T&Os: the Atlantic multidecadal oscillation (AMO) and the Niño-3.4 index for El Niño–Southern Oscillation (Niño-3.4).

AMO was first discovered by Schlesinger and Ramankutty (1994) and named by Kerr (2000), as a natural 60–80-yr cycle of sea surface temperatures across the North Atlantic Ocean. Despite its regional underpinnings, the AMO impacts climate across a broad swath of the globe (Knight et al. 2006; Sun et al. 2019). AMO data were obtained from the U.S. National Oceanic and Atmospheric Administration's Earth System Research Laboratory. Note that the dataset was collected in January 2019, and this dataset is updated monthly and detrended using a running mean filter. The Niño-3.4 is an oceanic-based quantification of the combined oceanic–atmospheric phenomenon known as El Niño–Southern Oscillation (ENSO). Possibly discovered as far back as the nineteenth century (see Wallace and Gutzler 1981), ENSO is an irregular (2–7 year) cycle of anomalous sea surface temperatures across a wide longitudinal band of the equatorial Pacific Ocean that alters SLP values in the atmosphere above it, setting off a cascade of various climate anomalies on a global scale. ENSO has been shown in previous research to heavily regulate global temperatures, with positive Niño-3.4 values usually leading to anomalously warm global temperatures (El Niños) and negative Niño-3.4 values leading to colder conditions (La Niñas). While the nonstandardized version of the Niño-3.4 index was obtained from the National Center for Atmospheric Research (NCAR) and the University Corporation for Atmospheric Research (UCAR), for use in this research, all Niño-3.4 data were standardized prior to analyses herein.

Monthly level global temperature data were obtained from U.S. National Aeronautics and Space Administration's Goddard Institute for Space Studies (GISS) Surface Temperature Analysis, version 4 (GISTEMP Team 2019; Lenssen et al. 2019). The global monthly mean combined land surface air and sea surface water temperature anomalies were collected and standardized for 1979–2018. For spatial analyses, the 2° × 2° gridded land–ocean temperature index was also acquired from GISS. Northern Hemisphere September sea ice extent data used for comparison purposes were retrieved from the National Centers for Environmental Information (please see Table S4).

To independently analyze trends in the near-surface variables that make up the GWTC2, monthly mean ERA5 (Hersbach et al. 2020) data were retrieved for the 0000, 0300, 0600, 0900, 1200, 1500, 1800, and 2100 UTC hours for the same six near-surface variables mentioned above (for the GWTC2) across the entire globe at 2° × 2° resolution. These were then turned into a single monthly value by averaging the eight hourly values for each of the 480 months from 1979 to 2018. Since air masses from the GWTC are based upon deseasonalized z scores for each location, data were then seasonally standardized by subtracting each value from the mean of the 40 monthly values and dividing each value by the standard deviation of the 40 monthly values (e.g., each January is subtracted from the mean of all Januaries and divided by the standard deviation of all Januaries).

Comparisons to previous indicators were made using the set of 26 metrics created by the Expert Team on Climate Change Detection and Indices (ETCCDI). These indices are often used by climate scientists to understand various temperature and precipitation trends around the globe, with a focus on extreme events (Alexander et al. 2006; Li et al. 2019). The annual gridded dataset for each of these were downloaded from the ETCCDI website (Climdex 2020) and turned into a global indicator by regridding the data to a 10 242-point equal-area grid to prevent oversampling the higher latitudes [using the GridSphere function in MATLAB from von Laven (2020)]. The mean index across this regridded domain was then computed for each of the 40 years, 1979–2018. This same regridding process was used to create global-scale averages of ERA5 data.

b. Calculation of climate indices

The development of the two GWTC2-based climate indices (GCIs) was a multistage process. First, the area covered (over the entire Earth's surface) for each AM on each day must be computed. Since AMs are computed on the native 0.5° × 0.5° latitude/longitude grid of the CFS/GWTC2, to avoid overrepresenting the higher-latitude AMs, binary values of AM occurrences at each location on each day were multiplied by the cosine of latitude for each location. Then, separately for each day in the time series and each of the 11 air masses, the products of this multiplication were summed (i.e., summed across latitude-adjusted space). This yields a 14 610 (days) by 11 (air masses) dataset representing the areal coverage (in latitude-adjusted km^2) across Earth's surface of each AM on each day, from 1 January 1979 to 31 December 2018. These areal coverages were then divided by the daily summed total of latitude adjusted space (165 010 km^2) to create percentages—which are representative of the total percent coverage of Earth's surface area (510 072 000 km^2) by each AM—that form the foundation for the computation of the two GCIs.

The second stage of the computation differs for the WCI and GEI. For the WCI, the percentages of the three cool AMs [humid cool (HC), cool (C), and dry cool (DC)] were summed, and subtracted from the summed percentages of the three warm AMs [humid warm (HW), warm (W), and dry warm (DW)] on each day (thus, positive values equate to greater areal coverage of the three warm AMs). For the GEI, the percentages of the four extreme AMs (or the corner AMs in Fig. 1; DW, DC, HW, and HC) were summed—each representing the most extreme ~5% of their respective corner of the multivariate temperature/humidity distribution (Lee 2020a).

The third stage in the calculation of the GCIs is standardization to the 1981–2010 climate normal period. The 1981–2010 median of each GCI is subtracted from each individual value in the time series, and this difference is divided by the 1981–2010 interquartile range, effectively creating robustly defined *z*-score-based indices. While both GCIs are available on a daily scale, for the results presented below, each GCI was averaged on a month-by-month basis for the 480 months between January 1979 and December 2018 to align with the time scale of most T&O data.

While the focus of the research are on these two global-scale indicators, for a more detailed analysis, other geographic partitions of these two indices were also calculated, including ocean-only, land-only, tropical (<23.5°N/S latitude), high-latitude (>66.5°N/S latitude), and midlatitude (≥23.5°N/S and ≤66.5°N/S).

c. Data analysis

Trends in global AM areal coverage, ERA5 climate variables, WCI, and GEI were computed using Theil–Sen slope estimations. This robust method of finding linear trends computes the median slope between all possible combinations of coordinate pairs [in this case the *x* coordinates are the month in the time series (from 1 to 480), and the *y* coordinate is the monthly value of either the individual climate variables, the index, or the percent coverage of an AM]. For air masses, WCI and GEI, bootstrap resampling was used to construct 95% confidence intervals using the bias corrected and accelerated percentile method, and then converted to *p* values using the method described in Altman and Bland (2011). For ERA5 climate variables, the nonparametric Mann–Kendall trend test was used to compute statistical significance. Decadal changes in these monthly level slopes were computed by multiplying the slopes by 120 (12 months yr^{-1} × 10 years decade^{-1}). Trends in individual gridpoint annual airmass occurrences and annual spatial GISS data were computed using simple linear regression, with *p* values of the slope coefficient used to control for the false detection ratio (as in Wilks 2016) to determine field significance. The associations between teleconnections and WCI, GEI, and AMs, were examined using either Spearman rank correlations, or, where necessary, a nonlinear (eta η) correlation. Annual-level associations between ETCCDI indicators and each index were computed using simple Pearson correlations, while partial Pearson correlations were used to examine the multivariate associations between the monthly scale indices and each ERA5 climate variable. All analyses were completed using MATLAB 2020a and associated toolboxes.

3. Results and discussion

a. Trends in AMs and GCIs

When multiplied by the surface area of Earth (510 072 000 km^2), the latitude-adjusted *percentage-point* (%-pts) changes of an AM equate to the change in an AM's areal coverage of Earth's surface (%-pts being the difference between the two percentages). While many of the slopes appear minimal in magnitude, in reality this represents a massive shift in areal coverage for the AMs over the period of study (Fig. 2). For example, the three warm types are increasing by a summed +13.8%-pts and the three cool types decreasing by about −11.5%-pts of surface area of Earth over this 40-yr period, which is a rate of +3.4%-pts decade^{-1} and −2.9%-pts decade^{-1}, respectively (Table 1). The warm air mass itself is increasing its spatial coverage at a rate of nearly 10 million km^2 decade^{-1}, an area roughly the size of Canada, largely at the expense of a 9.5 million km^2 decrease in area covered by the cool AM. Further, the time series of spatial extent of the three warm AMs all have strong and significant positive correlations with the surface temperature data (rho = 0.70, 0.82, 0.84 for DW, HW, and W), while the three cool AMs have strong and significant negative correlations (rho = −0.60, −0.71, −0.79 for HC, DC, and C, respectively; supplemental material). Additionally, the expanse of all nonseasonal (+0.7%-pts decade^{-1}, equating to 3.8 million km^2) AMs and the four extreme/corner AMs (+0.5%-pts decade^{-1}, 2.4 million km^2) are also increasing markedly. The three humid AMs (+2.0%-pts decade^{-1}; 10.0 million km^2) and the three dry AMs (−1.3%-pts, −6.7 million km^2) are trending in expected directions, as humid versus dry is categorized in the GWTC2 using 2-m dewpoint temperatures, which are expected to rise concurrent with temperatures, as a warmer atmosphere will accommodate more absolute water vapor content (O'Gorman and Schneider 2009). Of all the air masses, only the CFP has seen a statistically insignificant trend over this timeframe (−0.01%-pts decade^{-1}, $p = 0.100$).

The largest changes in most AMs occur in the tropics—especially the tropical oceans (Fig. 3), where some

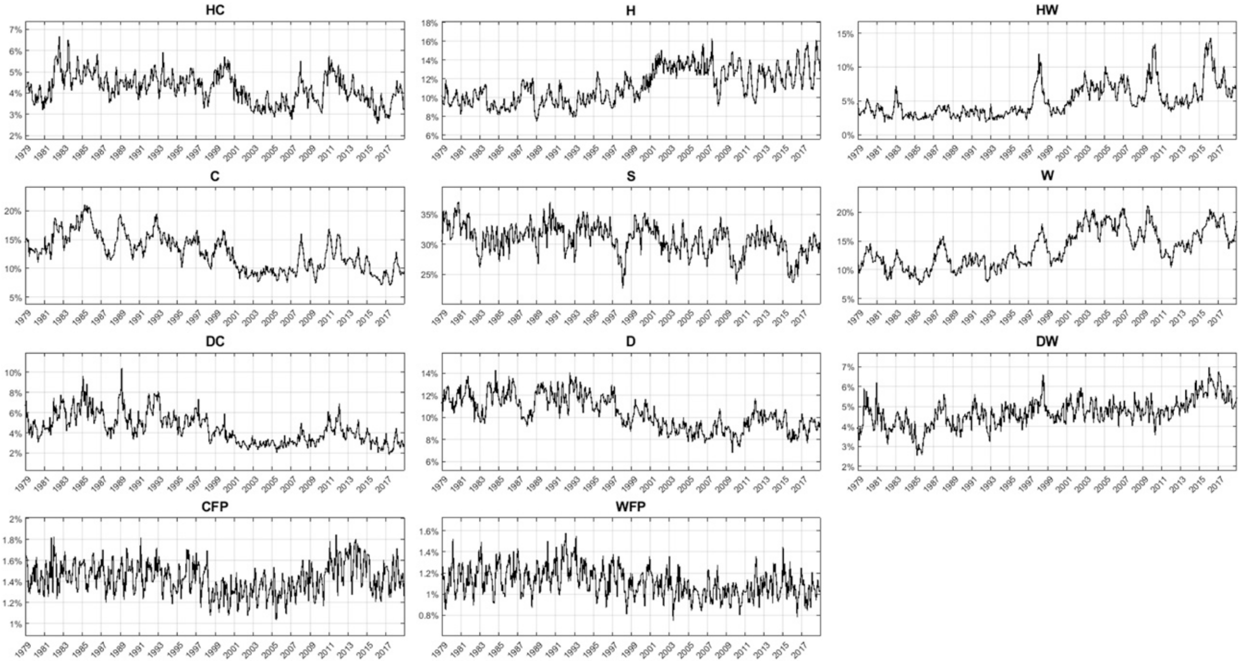

FIG. 2. Monthly time series of each GWTC2 AM's percentage coverage of Earth's surface.

of the warm AMs are occurring at a rate of nearly an extra 2 days every year (or about 80 more days per year over the 40-yr period). A secondary area of major change appears in the Arctic. Considering the largest changes in temperatures are generally known to be occurring in the Arctic (i.e., Arctic amplification; Francis and Vavrus 2012), the results for the tropics are somewhat surprising. However, when *standardized* (rather than anomalous) GISS temperature data are examined, the relative changes in tropical temperatures become much more apparent (Fig. 4) and mimics the results noted with the warm AMs. This result is due to the fact that the GWTC2 system uses standardized variables to compute AMs. While the trends in standardized temperature (or air masses derived with such) might be less important in a "global scope" than unstandardized anomalies, for humans, plants, and animals living in the tropics that have become acclimatized to an environment with minimal daily/annual meteorological variability or have extremely narrow ranges of tolerance, even seemingly minor absolute changes can have major impacts on ecosystems (Wiens 2016; Deutsch et al. 2008; Barron 1995).

The month-by-month time series of both GCIs are presented in Fig. 5. With the WCI, there appears to be a major shift toward a positive phase around 2000–01, after which the index does not drop below zero for more than a handful of consecutive months. The WCI has a statistically significant increasing trend ($m = 0.0031$, $+0.374\ \mathrm{decade}^{-1}$, $p < 0.001$) over the 480-month period of study, indicating that warmer AMs are increasing markedly at the expense of cooler AMs (Table 1). The GEI also shows a statistically significant secular increase ($m = 0.0016$, $+0.192\ \mathrm{decade}^{-1}$, $p < 0.001$), though to a lesser magnitude than what is noted with WCI. This is

TABLE 1. Trends in each AM and GCI. Theil–Sen slope [TSslope (m)] is based upon the 480 monthly values of percentage coverage of Earth's surface (for AMs), or the 480 monthly values of the GCIs; p is the p value of the slope; change decade^{-1} is the percentage point change in areal coverage per decade for AMs, or the change in value per decade for the GCIs (both calculated as $m \times 12 \times 10$; for the 12 months in a year and 10 years in a decade); $\mathrm{km}^2\ \mathrm{decade}^{-1}$ is the change in the amount of Earth's surface covered per decade (km^2 for each AM)—which is not applicable to the GCIs.

	TSslope (m)	p	Change decade^{-1}	$\mathrm{km}^2\ \mathrm{decade}^{-1}$
		GWTC2 air masses		
HC	−0.000 022	<0.001	−0.26%	−1 326 353
H	0.000 092	<0.001	1.10%	5 634 273
HW	0.000 093	<0.001	1.12%	5 708 182
C	−0.000 155	<0.001	−1.86%	−9 487 168
S	−0.000 073	<0.001	−0.88%	−4 493 069
W	0.000 163	<0.001	1.96%	9 995 761
DC	−0.000 063	<0.001	−0.75%	−3 850 064
D	−0.000 078	<0.001	−0.93%	−4 747 844
DW	0.000 030	<0.001	0.36%	1 836 142
CFP	−0.000 001	0.100	−0.01%	−56 876
WFP	−0.000 004	<0.001	−0.05%	−233 859
		GWTC2-based climate indices (GCIs)		
WCI	0.003 113 4	<0.001	0.374	—
GEI	0.001 598 0	<0.001	0.192	—

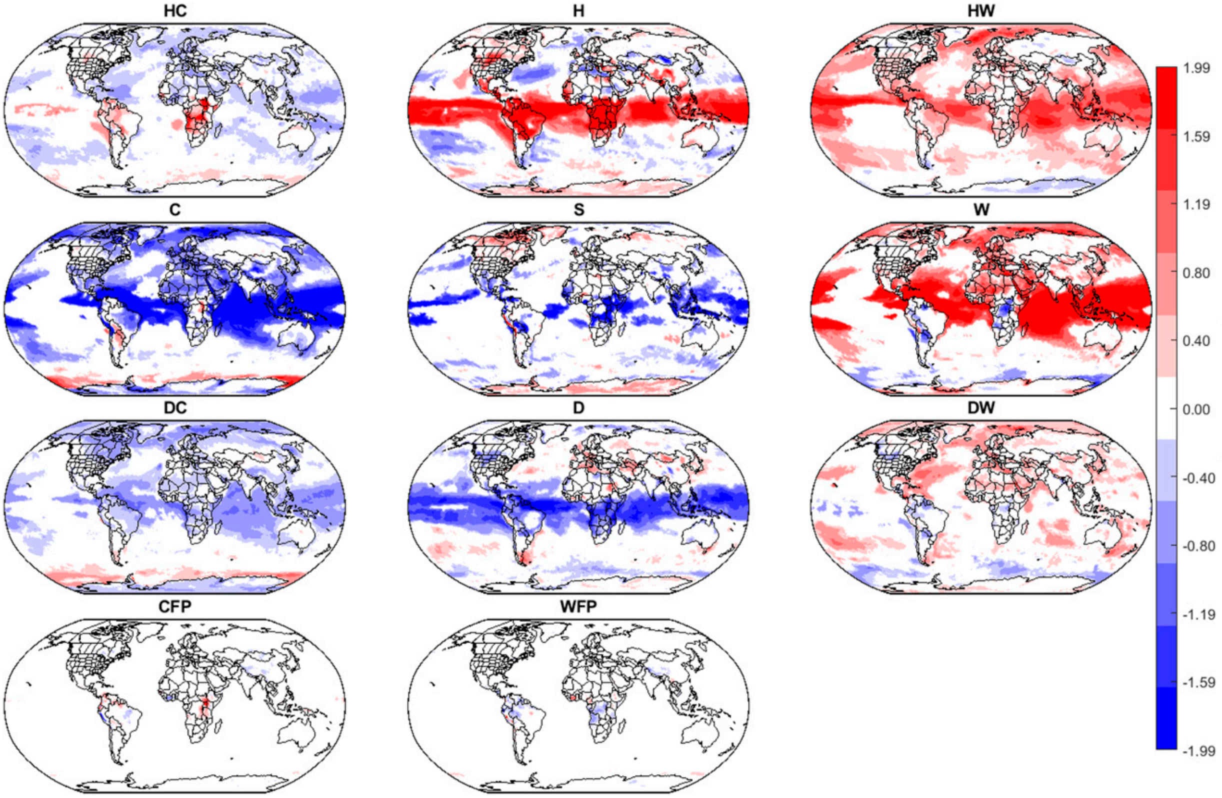

FIG. 3. Trend in occurrences per year of each of the 11 GWTC2 AMs. Only significant values are shown ($p < 0.05$).

likely due to two cool AMs (DC and HC) being included in this index, both of which show significant decreasing trends. Nonetheless, their inclusion in the calculation of the GEI is warranted, as it is the extreme events, rather than the mean, that are most impactful on society, including those on each end of the temperature spectrum (O'Neill and Ebi 2009; Hajat et al. 2007; Lee and Sheridan 2018; Sheridan et al. 2019). Both the WCI and the GEI are increasing more so over the ocean (WCI = $+0.390\,\mathrm{decade}^{-1}$, GEI = $+0.207\,\mathrm{decade}^{-1}$, both $p < 0.001$) than they are over land (WCI = $+0.265\,\mathrm{decade}^{-1}$, GEI = $+0.066\,\mathrm{decade}^{-1}$, both $p < 0.001$), however, the changes over land are arguably more impactful on human life. Latitudinally, the tropics and midlatitudes show much greater increases in both indices than the high latitudes, where the GEI actually shows a significant *decrease* ($-0.043\,\mathrm{decade}^{-1}$, $p = 0.03$). However, if the Antarctic is excluded, the Arctic shows an increasing trend in both indices, though only the WCI ($+0.334\,\mathrm{decade}^{-1}$; $p < 0.001$) is significant.

b. Associations with teleconnections and oscillations

When analyzed against the T&Os, the largest magnitude correlations are with the AMO (Fig. 6)—which exhibits a strong positive association with WCI (rho = 0.76, $p < 0.001$), and a weaker, but significant association with GEI (rho = 0.27, $p < 0.001$). Further, much like the trend toward warmer temperatures leading to higher WCI values, especially after 2000, the AMO also shows a considerable trend upward over the period of study, though beginning in the mid-1990s. This correlation is driven mostly by the strong positive correlations between AMO and the three warm types (DW, W, and HW), and a strong negative correlation between the AMO and all three cool types (DC, C, and HC)—all of which are statistically significant ($p < 0.05$; supplemental material). When mapped, the vast majority of the spatial correlations between airmass frequency and the WCI comes from the tropics, though a smaller secondary area of correlation is visible in Baffin Bay, and the Greenland, Iceland, and Norwegian Seas with the W, HW, and C air masses. Of the additional geographic partitions of the two indicators, GEI over the ocean and over the midlatitudes exhibited marginally stronger correlations with AMO than its global-scale counterpart; for WCI, the global-scale WCI–AMO relationship was the stronger than any other geographically partitioned WCI (Table S3).

Previous research has shown that the AMO plays a large role in Northern Hemisphere climate variability,

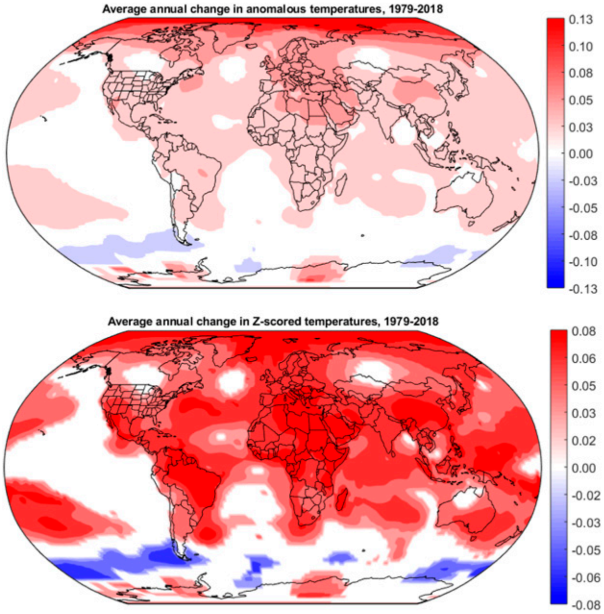

FIG. 4. (top) Trends in annual anomalous temperatures from GISS data, 1979–2018 (°C). (bottom) Trends in annual standardized anomalous temperatures from GISS data, 1979–2018 (in standard deviation units). Only significant values are shown ($p < 0.05$).

though it can also have global-scale impacts. Schlesinger and Ramankutty (1994) found that the AMO manifests in the global mean temperature record, and others have noted that due to its multidecadal-scale oscillation, the AMO can either mask or enhance the anthropogenically induced trend in global temperatures (Dima and Lohmann 2007). As noted in Knight et al. (2006, and references therein) the AMO also impacts rainfall patterns in Brazil and Africa, North Atlantic hurricanes, and summer climates on the adjacent European and North American continents, while Häkkinen et al. (2011) show a link between the AMO and large-scale atmospheric blocking events. Due to its strong oceanic–atmospheric coupling, fingerprints of the AMO can also be found to influence SST variability in the Arabian Sea, Indian Ocean, and the Pacific Ocean, along with near-surface temperature anomalies over Eurasia (Sun et al. 2019, 2017a,b). In one of the few papers examining the manifestation of the AMO in the Southern Hemisphere, Sun et al. (2018) describe the inverse relationship between northern and southern Atlantic SSTs stemming from ocean heat redistribution forced by changes in the Atlantic meridional overturning circulation.

Herein, with only a 40-yr period of record, the AMO exhibits a strong correlation to the global-scale temperature record (rho = 0.69, $p < 0.001$), though it is substantially weaker when the secular trend is removed (rho = 0.35, $p < 0.001$), and markedly lower than the correlation between detrended AMO and WCI (rho = 0.55; Fig. 6). Thus, while it is known that the AMO can modulate global temperatures, this research suggests that the AMO's role may be even greater in modulating the *multivariate* global weather, herein represented by the areal coverage of GWTC2 AMs.

Significant correlations between the raw GCIs and all other T&Os are much weaker, with only the EA pattern and ENSO showing an absolute correlation greater than rho = 0.25 with either the GEI or the WCI. When both the T&Os and GCIs are detrended, the PDO and ENSO exhibit a greater association with both indices than using nondetrended values, though these are still relatively weak. Of particular note is the apparent visual association between well-known ENSO events and the GEI shown in Fig. 5. For example, three of the four spikes in the GEI (i.e., where GEI > 2.0 in Fig. 5) occurred during three of the strongest El Niño events of the last several decades (1982–83, 1997–98, 2015–16), while the other one corresponds to one of the strongest La Niña events (2010–11), which would suggest a *u*-shaped relationship between GEI and Niño-3.4 (Fig. 7, top). Further, when geographical partitions of the indicators are examined, both tropical WCI and tropical GEI have slightly stronger rank correlations with Niño-3.4 than the global-scale versions. To help quantify the nonlinear association between the two, a nonlinear (eta η) correlation was run by partitioning the 480 monthly Niño-3.4 values into 10 ordered bins (with uniform width, as would be used in a histogram) of 48 values each (Fig. 7, top), which returned a statistically significant $\eta = 0.52$ ($p < 0.001$) between the raw Niño-3.4 and GEI data, and $\eta = 0.55$ ($p < 0.001$) using detrended Niño-3.4 and GEI data (Fig. 6). Further, the GEI is heavily impacted by the frequency of the HW air mass, especially in the tropical Pacific and Indian Oceans, and northern South America—which also points to the influence of ENSO impacting this index (Fig. S2). Eta correlations with other GEI/T&O combinations mostly yielded either weak relationships ($\eta < 0.30$) or similar absolute values to those derived from the more traditional Spearman's rho, indicating a fairly linear relationship.

Many previous studies have highlighted the link between ENSO phases and extreme weather. Using clustered patterns of sea surface temperatures, Alexander et al. (2009) found that extreme temperatures from as far away as Australia to southern Africa, Canada, and Siberia were all impacted by ENSO, though precipitation variability was less coherent. Examining multiple T&Os, Kenyon and Hegerl (2010) found extreme precipitation events on at least 5 continents were substantially impacted by ENSO. In a rare multivariate analysis, Hao et al. (2018) found that ENSO phases impacted the

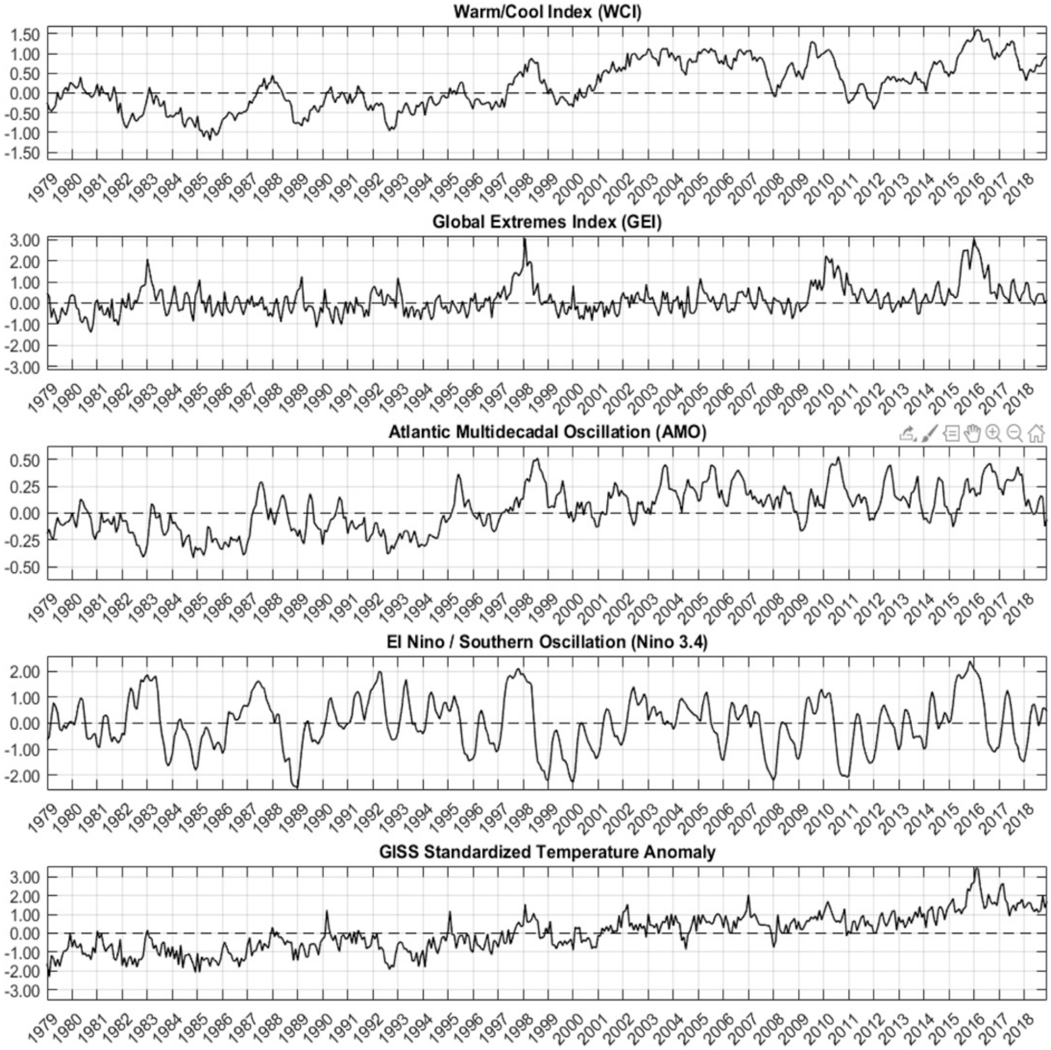

FIG. 5. The monthly time series of the two GCIs (WCI and GEI), two selected T&Os (AMO and Niño-3.4), and the standardized global temperature anomaly [GISS(z)], 1979–2018.

frequency of combined dry and hot events in parts of South and Central America, Africa, Asia, Alaska, and Australia during their respective warm seasons. Beyond the two major meteorological variables, other research has found links between ENSO and wind events in parts of the United States (Enloe et al. 2004), surface pressure in Europe (Fraedrich and Müller 1992), and high clouds throughout much of the globe (Li et al. 2017). And, using the previous version of the GWTC (the GWTC1; Lee 2014), Lee (2016) found ENSO to have a significant impact on cold-season AM frequencies in the southern half of the United States and most of Mexico.

c. *Index associations with existing climate indicators*

To establish these new GWTC2-based indices as global climate indicators, the WCI and GEI were first examined against the standardized monthly surface temperature anomaly record from GISS data. Of the two indices, WCI expectedly showed the stronger relationship (rho = 0.85, $p < 0.001$), and is on par with the correlation between global temperatures and other climate indicators. For example, Northern Hemisphere September sea ice extent—considered a more traditional climate indicator—and GISS annual mean surface temperature anomaly data have a Spearman correlation of rho = −0.84; correspondingly, annually averaged WCI also exhibits a strong association (rho = −0.70) with sea ice extent. The GEI also displayed a moderate association with the surface temperature record (rho = 0.41, $p < 0.001$), especially when nonlinear associations (Fig. 7, bottom) were computed ($\eta = 0.54$, $p < 0.001$)—stronger than with any of the teleconnections

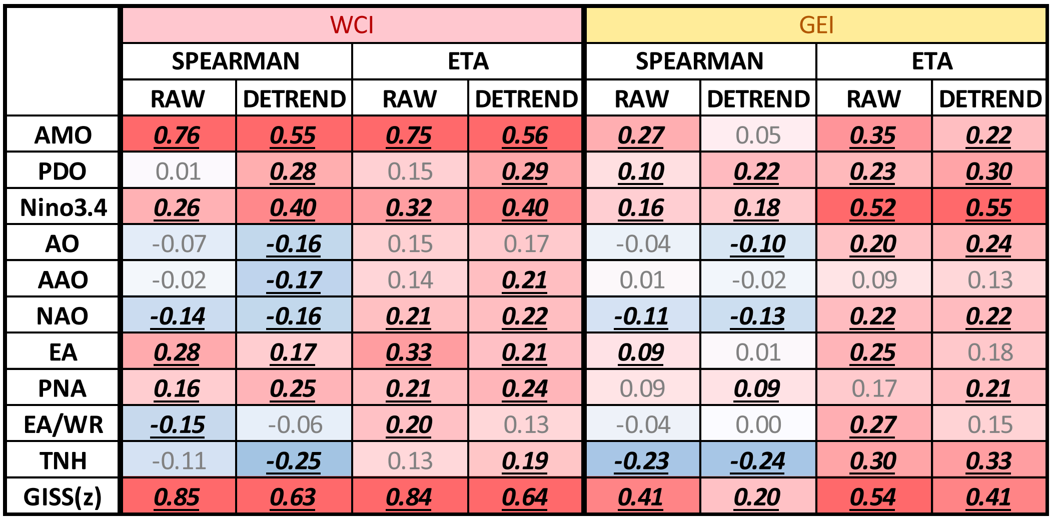

	WCI				GEI			
	SPEARMAN		ETA		SPEARMAN		ETA	
	RAW	DETREND	RAW	DETREND	RAW	DETREND	RAW	DETREND
AMO	***0.76***	***0.55***	***0.75***	***0.56***	***0.27***	0.05	***0.35***	***0.22***
PDO	0.01	***0.28***	0.15	***0.29***	***0.10***	***0.22***	***0.23***	***0.30***
Nino3.4	***0.26***	***0.40***	***0.32***	***0.40***	***0.16***	***0.18***	***0.52***	***0.55***
AO	-0.07	***-0.16***	0.15	0.17	-0.04	***-0.10***	***0.20***	***0.24***
AAO	-0.02	***-0.17***	0.14	***0.21***	0.01	-0.02	0.09	0.13
NAO	***-0.14***	***-0.16***	***0.21***	***0.22***	***-0.11***	***-0.13***	***0.22***	***0.22***
EA	***0.28***	***0.17***	***0.33***	***0.21***	***0.09***	0.01	***0.25***	0.18
PNA	***0.16***	***0.25***	***0.21***	***0.24***	0.09	***0.09***	0.17	***0.21***
EA/WR	***-0.15***	-0.06	***0.20***	0.13	-0.04	0.00	***0.27***	0.15
TNH	-0.11	***-0.25***	0.13	***0.19***	***-0.23***	***-0.24***	***0.30***	***0.33***
GISS(z)	***0.85***	***0.63***	***0.84***	***0.64***	***0.41***	***0.20***	***0.54***	***0.41***

FIG. 6. Spearman correlations and nonlinear eta correlations between each GCI and selected T&Os (rows) for both raw data and detrended data. Statistically significant values ($p < 0.05$) are bolded, italicized, and underlined, whereas nonsignificant values are gray. For Spearman correlations, darker reds (blues) mean increasingly positive (negative) correlations. Eta correlations can only be positive, and thus, darker reds equate to stronger associations. GISS(z) is the standardized surface temperature anomaly. All statistics are based upon 1979–2018.

when examining raw data. Spatially, both indices exhibit widespread correlations with temperature anomalies (Fig. 8). The WCI is most highly associated with temperatures throughout much of the Atlantic Ocean, especially the tropical Atlantic, northern South America, tropical Africa, and most of the Indian Ocean north of 30°S. The GEI has a similar spatial pattern of correlations with the GISS temperature anomaly dataset, though lower in magnitude and shifted westward in most ocean basins. This essentially means that the WCI and, to a lesser extent, the GEI are most impacted by the trends and variability in global temperatures in the tropical oceans, central Africa, and northern South America. This aligns well with the areas of Fig. 3 where air masses are changing the most, and Fig. 4 (bottom) where standardized anomalies are changing the most. While the WCI correlates well with the temperature record over the entire 40-yr period of record, there is noted variability in these correlations during certain blocks of time (e.g., 1986, 1993, 2000, 2002, 2005, 2014, and 2016–18 when shorter-term correlations between WCI and GISS approach $r < 0.0$; Fig. 9). These ephemeral changes in association imply that changes in other meteorological variables (humidity, wind, SLP or cloud cover that comprise the GWTC2) are driving changes in air masses that are not reflecting similarly in the global surface temperature record.

In fact, beyond temperatures there are multiple surface climate variables exhibiting significant changes in the equatorial Pacific and Atlantic Oceans, and in the southeastern Pacific Ocean (Fig. 10). These changes include increased cloud cover, a slight cooling, decreased dewpoints, an increase in SLP in the eastern South Pacific, and a strengthening of the southeast trade winds—all results noted elsewhere (e.g., Zhou et al. 2016). This increased easterly wind speed is leading to an enhanced La Niña effect, with increasingly warm and humid conditions in the western equatorial Pacific and northern Indian Oceans. Some of these changes could be due to increased sulfate aerosols—both natural and anthropogenic in these areas (Takahashi and Watanabe 2016), which would favor increased cloudiness (due to an abundance of cloud condensation nuclei; Williamson et al. 2019), and lead to cooler temperatures (perhaps due to increased reflection of insolation from cloud cover) and lowering dewpoints. The colder air temperatures over the eastern South Pacific would result in increasing SLP off the west coast of South America, which would facilitate the stronger trade winds as well.

While the *air masses* underlying the WCI and GEI are multivariate in nature, partial correlations were calculated in order to determine if the *indices* themselves represent the multivariate changes in the climate system. Table 2 shows partial correlations between the WCI/GEI and the globally averaged values of the near surface variables obtained from ERA5. For WCI, while temperature shows the strongest correlation when controlling for each of the other variables, dewpoints, SLP, zonal winds, and wind speed all show significant ($p < 0.05$) contributions to WCI variability; overall the variables account for 82% of WCI variability. Of note, the dewpoint has a negative partial correlation with WCI, indicating that, despite the high

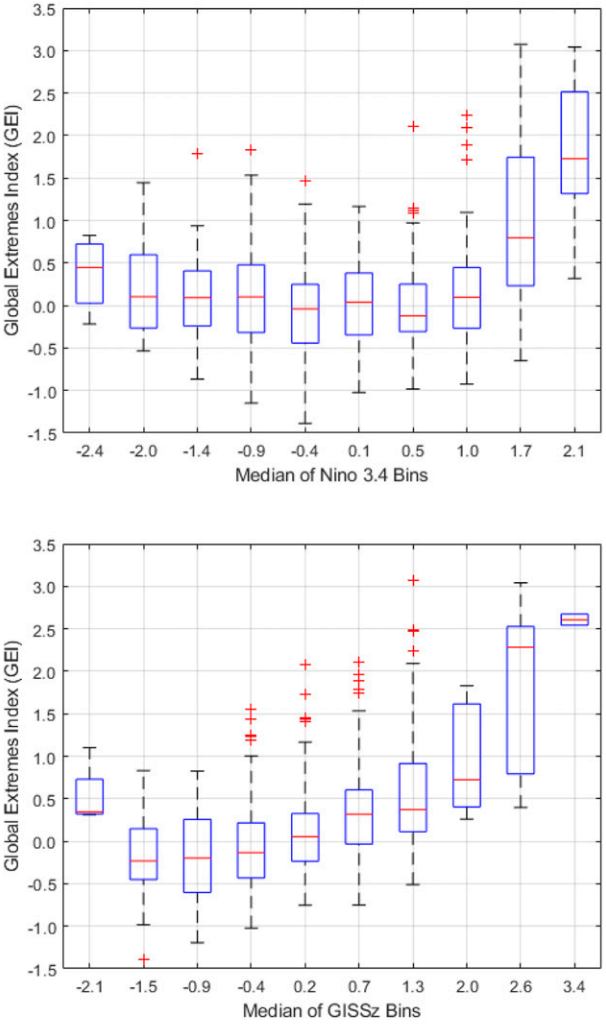

FIG. 7. Box-and-whisker plots showing nonlinear relationship (top) between GEI data and Niño-3.4 and (bottom) between GEI data and GISS(z). The y axis on both plots is the GEI data within each of the 10 ordered equal-spaced bins of the standardized Niño-3.4 index or GISS(z) (x axes), with the bins labeled by their median values. Red lines are medians, boxes are the interquartile ranges, whiskers cover about ±2.7 standard deviations from the mean, and the red + symbols are individual outlier data points.

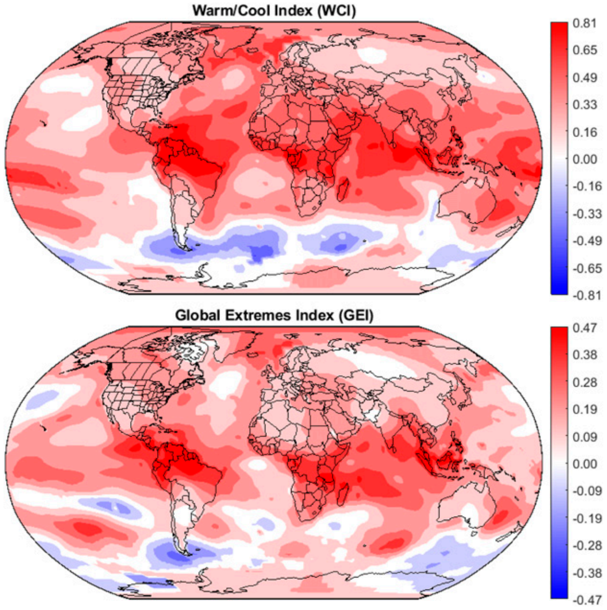

FIG. 8. Spearman correlations between the monthly GISS surface temperature anomalies and the (top) WCI and (bottom) GEI. Note the difference of scale in the two color bars.

degree of correlation between temperature and dewpoints in most locations, areas of the globe where these trends are diverging (e.g., warming and drying, in the equatorial Pacific, the southwestern United States, eastern Australia, parts of southern Africa, and the Middle East), are significantly impacting the WCI. For GEI, the variables combined to account for considerably less variability in the index ($R^2 = 0.34$), with temperature, zonal and meridional winds, and cloud cover each being significant factors. Overall, the areas that are showing the most significant trends in these surface variables (the tropics) are the same regions that are most highly correlated with WCI and GEI (Fig. 11), indicating that where there are multivariate changes, the WCI and GEI are incorporating them.

A thorough examination of the WCI's and GEI's suitability as new indicators also necessitates a comparison to existing indicators. In general, the WCI showed fairly strong correlations with all of the temperature-based ETCCDI metrics, especially TN90p and TX90p, which are measures of days exceeding the 90th percentile of minimum and maximum daily temperatures, respectively; both exhibited $r > 0.86$ (Table 3). By contrast, the WCI performs poorer with precipitation-based ETCCDI indicators, with only R99p (the summed amount of precipitation on the wettest days) having an $r > 0.5$ with WCI. These results are not altogether unsurprising considering that 1) the WCI is based on a warm versus cold airmass dichotomy, and 2) the air masses do not directly incorporate precipitation. This said, the GEI, performs much better with nearly every precipitation-based indicator and has a more consistent association across all ETCCDI indicators than WCI. For six of the nine precipitation-based indicators, the GEI exhibits $r > 0.5$, and has $r > 0.6$ for three of them. This is likely due to the known association between global precipitation (especially tropical precipitation) and ENSO (Dai and Wigley 2000; Curtis et al. 2007), with which the GEI has also been shown herein to strongly associate. Since the ETCCDI indicators are particularly focused on extreme events (Alexander et al. 2006), this consistency across these different metrics helps highlight the GEI's sensitivity to multiple climate extremes.

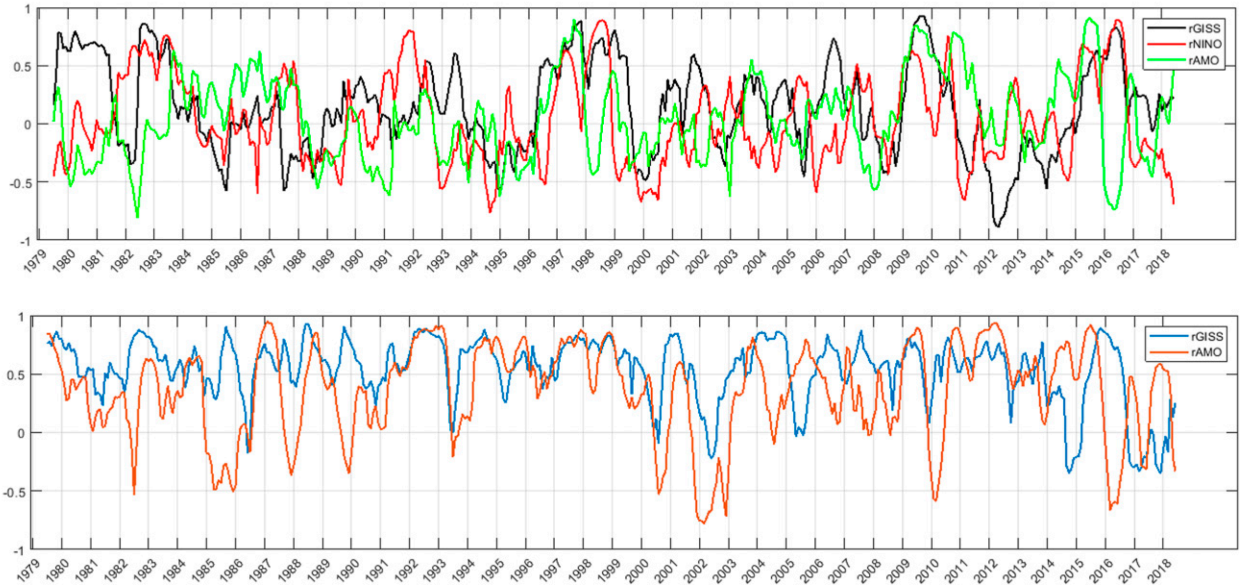

FIG. 9. (top) Centered 13-month moving correlations between GEI and GISS (black), between GEI and AMO (green), and between GEI and the Niño-3.4 index (red), 1979–2018. (bottom) Centered 13-month moving correlations between WCI and GISS (blue), and between WCI and AMO (orange), 1979–2018.

Taken together, these results present a number of key findings with regard to the WCI and GEI as climate indicators. First, the WCI shows promise as an indicator of the global climate, as it has 1) increased in the expected direction with overall global temperatures over the past four decades, 2) has a very strong association with the surface temperature record—a necessary hallmark of any metric to be considered a climate indicator, and 3) is strongly correlated with existing extreme thermal climate indicators. The GEI might also show promise as an indicator of global climate due to 1) its moderate nonlinear association with the GISS temperature data, 2) the fact that it is explicitly derived from climatological extremes, an arguably more-important potential impact of a changing climate, and 3) it is consistently associated with the suite of existing ETCCDI indicators, especially the precipitation-based indices. Further, both indices show significant spatial correlations with multiple climate variables in the same global locations where these variables are trending the most.

The results also support the added value of the WCI, in that it is indexing a unique *multivariate* component of the climate system (geographically and seasonally relative weather types or synoptic-scale air masses) that are undergoing changes concurrently with the background trend in global mean temperatures, but also are subjected to variability somewhat independently from it. In addition to the uniqueness, these AMs—and by extension these two indices—are also important, as they are key drivers regulating the extratropical atmosphere. Air masses have been shown in previous research to affect various biometeorological outcomes, especially human health and temperature-related mortality (Lee 2015; Hondula et al. 2014), as it is the synergy of the entire ‘‘weather situation’’ someone is exposed to (especially the interactions of temperature, humidity, and wind speed) that impacts thermal comfort, more so than individual meteorological variables acting in isolation.

Finally, as mentioned above, since their underlying air masses are based upon *standardized* anomalies (as opposed to *raw* anomalies), the WCI and GEI are able incorporate the multiple climatic changes happening in the tropics (where raw anomalies are smaller, but relative to the limited climatic variability there, large changes are happening for multiple variables) in addition to other parts of the globe.

One limitation of this study stems from some data-sparse regions of the globe. For example, in central Africa, using CFS data (from which the GWTC2 air masses are defined), trends in this region show a slight cooling and increased dewpoints, which lead to a significant rise in HC frequency. However, using a newer reanalysis product (ERA5), this same area shows significant warming and drying, a result that would not support increased HC frequency. This said, for the majority of the globe, the trends in air masses and the trends in ERA5 data are in agreement, minimizing the impact on the two indices. Nonetheless, differences between historical reanalysis based datasets and their potential influence on airmass identification should be explored in future research.

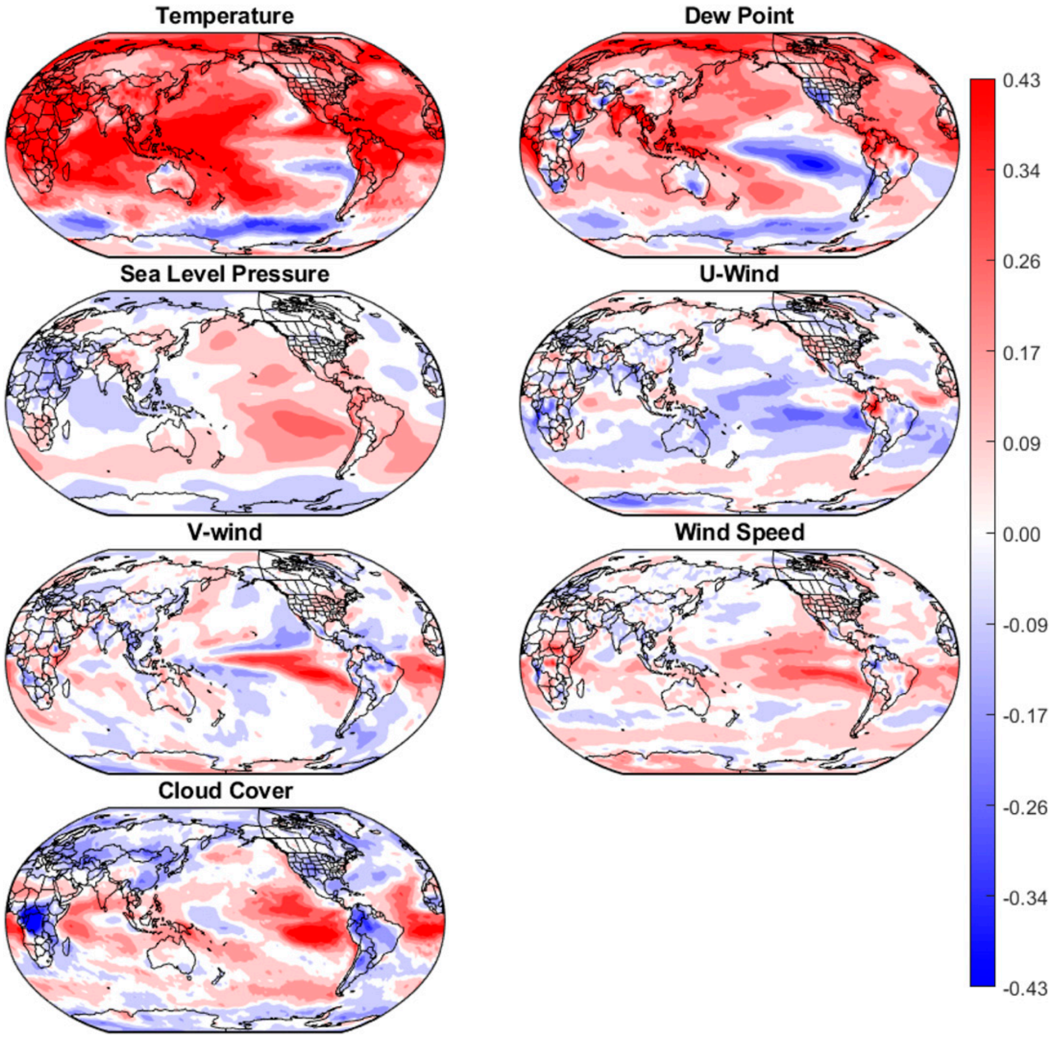

FIG. 10. The Theil–Sen slope estimate of each of the seasonally and geographically standardized ERA5 variables. Units are standard deviation units (z) per decade.

4. Conclusions

This research analyzes trends and variability in a recently developed dataset of global-scale multivariate air masses (the GWTC2) and develops two climate change indicators: the warm/cool index (WCI) and the global extremes index (GEI). These indices were then compared to trends in multiple near-surface climate variables and preexisting climate indicators (to examine their suitability as indicators) and to teleconnection data over a 40-yr period (to examine the impact of internal variability).

Results show that both indices have increased significantly since 1979 and hold promise as nontraditional indicators of the global climate, as both show a moderate (GEI) to strong (WCI) association with the global temperature record. While the WCI and GEI show land/ocean and latitudinal differences in their trends, the global-scale indices are thought to be better indicators of *global* climate change. Comparisons to various teleconnections reveal that the WCI is also strongly related to the AMO. While the AMO is an oscillatory phenomenon (rather than trending), the multidecadal scale of the AMO's cycle results in a general increase over much of the period of study. When detrended values of both indices are examined, the correlation between them decreases, but remains significant, suggesting that the AMO still greatly impacts near-surface multivariate weather variability on a global scale.

For the GEI, while correlations with the global temperature dataset were only moderate, the GEI's suitability as a unique climate indicator may be enhanced due to its ability to incorporate the *nonlinear* relationship to global temperatures, and its focus on extremes—that is, it is an

TABLE 2. Partial Pearson correlation (PartialCorr) coefficients between WCI or GEI and the global-scale averaged monthly value of each near-surface variable obtained from ERA5. RSQ is the R^2 of the multiple regression model with each of these variables are predictors. Statistically significant ($p < 0.05$) correlations are bolded and italicized.

PartialCorr	WCI	GEI
Temperature	***0.668***	***0.268***
Dewpoint	***−0.155***	−0.011
Sea level pressure	***0.127***	−0.057
U wind	***−0.187***	***0.091***
V wind	0.045	***−0.149***
Wind speed	***−0.145***	−0.072
Cloud cover	0.018	***0.120***
RSQ	0.818	0.344

indicator of extreme change even more than an indicator for changes in climatic means. The GEI exhibits a moderate nonlinear relationship with ENSO as well, which is most notable during particularly strong ENSO events (both warm phase and cool phase), underscoring the known impact ENSO has on global extremes. While the GEI shows moderate associations with both the Niño-3.4 and the surface temperature record, there is considerable variability in this index that is ‘‘unexplained,’’ at least by the evaluation herein.

Both indices are strongly impacted by variability in the tropics, especially the tropical oceans. In these areas, while trends in raw anomalies of temperature are small, due to the minimal seasonal and interannual variability of the tropics, trends in *standardized* anomalies in temperature are significant, and changes in multiple other near-surface variables (SLP, cloud cover, and winds) are even more substantial. Both the GEI and WCI are sensitive to these changes (in multiple different standardized climate variables), which are arguably as important as absolute temperature trends within the scope of changes to the climate system as a whole. Further, the WCI and GEI are significantly correlated with existing extreme climate change indicators. The WCI is strongly related to multiple thermal climate indicators but shows markedly lower associations with precipitation-based indicators. The GEI has a more consistent relationship across the indicators, and generally associates more strongly with precipitation-based indicators of change.

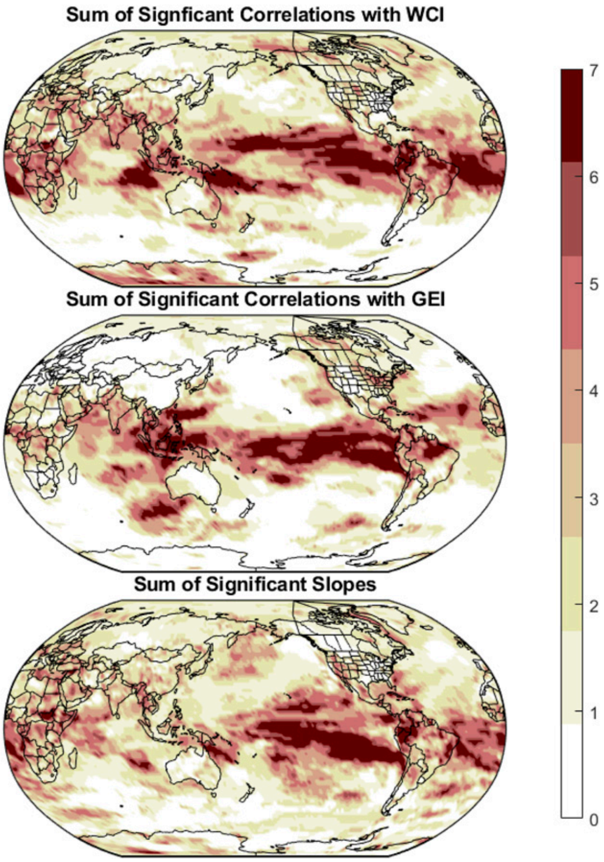

FIG. 11. The sum of statistically significant ($p < 0.05$) results at each grid point for (top) Pearson correlations between each of the ERA5 variables and WCI, (middle) the Pearson correlations between each of the ERA5 variables and GEI, (bottom) and the Theil–Sen slope estimates for each of the ERA5 variables.

When investigating the impacts of climate change, we are really asking how is the climate going to be different? What is ‘‘different’’ is always going to be relative; it is relative to the location, it is relative to the time of the year (e.g., increasingly warm winters, versus just increasingly warm year-round), it is relative to the usual amount of climate variability that one is accustomed to (for the location and time of year), and it can manifest in a variety of different climate variables. These indicators attempt to incorporate all of these aspects of climate change. While many published indicators of global climate are based upon a *single variable*, the two indices presented herein are fairly unique in that they are representative of the trends in the *multivariate* weather conditions—or air masses—that are experienced near Earth’s surface, while also being global in scope. No previously published indicators of climate change have explicitly examined trends in air masses, key drivers of the extratropical weather where nearly half of the world’s population lives, and important regulators of human thermal comfort. The air masses are also seasonally and geographically relative and incorporate the variability of the surface weather (using standardized anomalies rather than raw anomalies), adding levels of originality to the two indicators.

With the underlying data for these two indices (the GWTC2) are currently available online, regularly updated, and forecast out to 60 days, future work will automate

TABLE 3. Pearson correlations between each of the 26 ETCCDI indicator metrics and either the WCI or GEI. Precipitation-based indicators are CDD, CWD, PRCPTOT, R10mm, R20mm, R95p, R99p, Rx1day, Rx5day, and SDII. All other indicators are temperature-based. Statistically significant ($p < 0.05$) correlations are bolded and italicized. More details on these indices can be found in the supplemental material (Table S5) or at https://www.climdex.org/.

ETCCDI indicator	WCI	GEI
CDD	***−0.507***	***−0.548***
CSDI	***−0.364***	−0.140
CWD	***−0.448***	−0.067
DTR	***−0.384***	***−0.423***
FD	***−0.508***	***−0.502***
GSL	0.115	***0.343***
ID	−0.175	−0.299
PRCPTOT	0.076	***0.523***
R10mm	0.075	***0.527***
R20mm	0.024	***0.489***
R95p	***0.479***	***0.681***
R99p	***0.516***	***0.651***
Rx1day	***0.330***	***0.601***
Rx5day	0.073	***0.476***
SDII	0.139	***0.389***
SU	***0.615***	***0.462***
TN10p	***−0.774***	***−0.425***
TN90p	***0.871***	***0.587***
TNn	0.299	***0.358***
TNx	***0.472***	***0.321***
TR	***0.541***	***0.538***
TX10p	***−0.766***	−0.302
TX90p	***0.865***	***0.516***
TXn	***0.354***	***0.341***
TXx	***0.637***	***0.489***
WSDI	***0.816***	***0.557***

the calculation of these indices and keep historical records and forecasts of them freely available online. Additionally, future research could benefit by extending the GWTC2 classification to GCM data and examining the trends in these indices in historical and future global climate model output.

Acknowledgments. This research was partially supported by Federal Award NA17OAR4310159, entitled "Developing extreme event climate change indicators related to human thermal comfort" from the U.S. National Oceanic and Atmospheric Administration's Climate Program Office. The funding organization had no role in the conceptualization, design, data collection, analysis, decision to publish, or preparation of this manuscript. The author would also like to thank the editor and the three anonymous reviewers for their helpful comments, which have led to a greatly improved manuscript. The author declares no competing interests, financial or otherwise. CCL was responsible for the conceptualization, design, data collection, analysis, and writing of this manuscript.

Data availability statement. The datasets generated during and/or analyzed during the current study are available in the Mendeley Data repository. The WCI and GEI are available online (https://doi.org/10.17632/fvtznwrgsv.2; Lee 2020c). All GWTC2 data are available online (https://doi.org/10.17632/gbwwksnd6j.2; Lee 2020b). All GWTC2 data are also available at http://www.personal.kent.edu/~cclee/gwtc2global.html, or by contacting the author at cclee@kent.edu. All T&O data, ETCCDI data, and GISS temperature data can be acquired from their original sources (listed in Tables S4 and S5) or by contacting the author.

REFERENCES

Alexander, L. V., and Coauthors, 2006: Global observed changes in daily climate extremes of temperature and precipitation. *J. Geophys. Res.*, **111**, D05109, https://doi.org/10.1029/2005JD006290.

——, P. Uotila, and N. Nicholls, 2009: Influence of sea surface temperature variability on global temperature and precipitation extremes. *J. Geophys. Res.*, **114**, D18116, https://doi.org/10.1029/2009JD012301.

Altman, D. G., and J. M. Bland, 2011: How to obtain the P value from a confidence interval. *BMJ*, **343**, d2304, https://doi.org/10.1136/bmj.d2304.

Barron, E. J., 1995: Tropical climate stability and implications for the distribution of life. *Effects of Past Global Change on Life*, National Academies Press, 108–117.

Climdex, 2020: Gridded climate data. Accessed 10 April 2020, https://www.climdex.org/access/gridded/.

Curtis, S., A. Salahuddin, R. F. Adler, G. J. Huffman, G. Gu, and Y. Hong, 2007: Precipitation extremes estimated by GPCP and TRMM: ENSO relationships. *J. Hydrometeor.*, **8**, 678–689, https://doi.org/10.1175/JHM601.1.

Dai, A., and T. M. L. Wigley, 2000: Global patterns of ENSO-induced precipitation. *Geophys. Res. Lett.*, **27**, 1283–1286, https://doi.org/10.1029/1999GL011140.

Deutsch, C. A., J. J. Tewksbury, R. B. Huey, K. S. Sheldon, C. K. Ghalambor, D. C. Haak, and P. R. Martin, 2008: Impacts of climate warming on terrestrial ectotherms across latitude. *Proc. Natl. Acad. Sci. USA*, **105**, 6668–6672, https://doi.org/10.1073/pnas.0709472105.

Dima, M., and G. Lohmann, 2007: A hemispheric mechanism for the Atlantic multidecadal oscillation. *J. Climate*, **20**, 2706–2719, https://doi.org/10.1175/JCLI4174.1.

Enloe, J., J. J. O'Brien, and S. R. Smith, 2004: ENSO impacts on peak wind gusts in the United States. *J. Climate*, **17**, 1728–1737, https://doi.org/10.1175/1520-0442(2004)017<1728:EIOPWG>2.0.CO;2.

Fraedrich, K., and K. Müller, 1992: Climate anomalies in Europe associated with ENSO extremes. *Int. J. Climatol.*, **12**, 25–31, https://doi.org/10.1002/joc.3370120104.

Francis, J. A., and S. J. Vavrus, 2012: Evidence linking Arctic amplification to extreme weather in mid-latitudes. *Geophys. Res. Lett.*, **39**, L06801, https://doi.org/10.1029/2012GL051000.

GISTEMP Team, 2019: GISS Surface Temperature Analysis (GISTEMP), version 4. NASA Goddard Institute for Space Studies, accessed 21 August 2019, https://data.giss.nasa.gov/gistemp/.

Hajat, S., R. S. Kovats, and K. Lachowycz, 2007: Heat-related and cold-related deaths in England and Wales: Who is at risk? *Occup. Environ. Med.*, **64**, 93–100, https://doi.org/10.1136/oem.2006.029017.

Häkkinen, S., P. B. Rhines, and D. L. Worthen, 2011: Atmospheric blocking and Atlantic multidecadal ocean variability. *Science*, **334**, 655–659, https://doi.org/10.1126/science.1205683.

Hao, Z., F. Hao, V. P. Singh, and X. Zhang, 2018: Quantifying the relationship between compound dry and hot events and El Niño–Southern Oscillation (ENSO) at the global scale. *J. Hydrol.*, **567**, 332–338, https://doi.org/10.1016/j.jhydrol.2018.10.022.

Hersbach, H., and Coauthors, 2020: The ERA5 global reanalysis. *Quart. J. Roy. Meteor. Soc.*, **146**, 1999–2049, https://doi.org/10.1002/qj.3803.

Hondula, D. M., J. K. Vanos, and S. N. Gosling, 2014: The SSC: A decade of climate–health research and future directions. *Int. J. Biometeor.*, **58**, 109–120, https://doi.org/10.1007/s00484-012-0619-6.

Kenyon, J., and G. C. Hegerl, 2010: Influence of modes of climate variability on global precipitation extremes. *J. Climate*, **23**, 6248–6262, https://doi.org/10.1175/2010JCLI3617.1.

Kerr, R. A., 2000: A North Atlantic climate pacemaker for the centuries. *Science*, **288**, 1984–1985, https://doi.org/10.1126/science.288.5473.1984.

Knight, J. R., C. K. Folland, and A. A. Scaife, 2006: Climate impacts of the Atlantic multidecadal oscillation. *Geophys. Res. Lett.*, **33**, L17706, https://doi.org/10.1029/2006GL026242.

Lee, C. C., 2014: The development of a gridded weather typing classification scheme. *Int. J. Climatol.*, **35**, 641–659, https://doi.org/10.1002/joc.4010.

——, 2015: A systematic evaluation of the lagged effects of spatiotemporally relative surface weather types on wintertime cardiovascular-related mortality across 19 US cities. *Int. J. Biometeor.*, **59**, 1633–1645, https://doi.org/10.1007/s00484-015-0970-5.

——, 2016: Reanalysing the impacts of atmospheric teleconnections on cold-season weather using multivariate surface weather types and self-organizing maps. *Int. J. Climatol.*, **37**, 3714–3730, https://doi.org/10.1002/joc.4950.

——, 2020a: The gridded weather typing classification version 2: A global scale expansion. *Int. J. Climatol.*, **40**, 1178–1196, https://doi.org/10.1002/JOC.6263.

——, 2020b: GWTC2 Dataset—A global-scale classification of air masses, version 2. Mendeley Data, accessed 2 July 2020, https://doi.org/10.17632/gbwwksnd6j.2.

——, 2020c: Global Air Mass Climate Indicators—Warm/cool index and global extremes index. Mendeley Data, V2, accessed 2 July 2020, https://doi.org/10.17632/fvtznwrgsv.2.

——, and S. C. Sheridan, 2018: A new approach to modeling temperature-related mortality: Non-linear autoregressive models with exogenous input. *Environ. Res.*, **164**, 53–64, https://doi.org/10.1016/j.envres.2018.02.020.

Lenssen, N., G. Schmidt, J. Hansen, M. Menne, A. Persin, R. Ruedy, and D. Zyss, 2019: Improvements in the GISTEMP uncertainty model. *J. Geophys. Res. Atmos.*, **124**, 6307–6326, https://doi.org/10.1029/2018JD029522.

Li, K. F., H. Su, S. N. Mak, T. M. Chang, J. H. Jiang, J. R. Norris, and Y. L. Yung, 2017: An analysis of high cloud variability: Imprints from the El Niño–Southern Oscillation. *Climate Dyn.*, **48**, 447–457, https://doi.org/10.1007/s00382-016-3086-7.

Li, Z., X. Li, Y. Wang, and S. M. Quiring, 2019: Impact of climate change on precipitation patterns in Houston, Texas, USA. *Anthropocene*, **25**, 100193, https://doi.org/10.1016/j.ancene.2019.100193.

O'Gorman, P. A., and T. Schneider, 2009: The physical basis for increases in precipitation extremes in simulations of 21st-century climate change. *Proc. Natl. Acad. Sci. USA*, **106**, 14 773–14 777, https://doi.org/10.1073/pnas.0907610106.

O'Neill, M. S., and K. L. Ebi, 2009: Temperature extremes and health: Impacts of climate variability and change in the United States. *J. Occup. Environ. Med.*, **51**, 13–25, https://doi.org/10.1097/JOM.0b013e318173e122.

Saha, S., and Coauthors, 2010: The NCEP Climate Forecast System Reanalysis. *Bull. Amer. Meteor. Soc.*, **91**, 1015–1058, https://doi.org/10.1175/2010BAMS3001.1.

——, and Coauthors, 2014: The NCEP Climate Forecast System version 2. *J. Climate*, **27**, 2185–2208, https://doi.org/10.1175/JCLI-D-12-00823.1.

Schlesinger, M. E., and N. Ramankutty, 1994: An oscillation in the global climate system of period 65–70 years. *Nature*, **367**, 723–726, https://doi.org/10.1038/367723a0.

Sheridan, S. C., C. C. Lee, and M. J. Allen, 2019: The mortality response to absolute and relative temperature extremes. *Int. J. Environ. Res. Public Health*, **16**, 1493, https://doi.org/10.3390/ijerph16091493.

Sun, C., F. Kucharski, J. Li, F. F. Jin, I. S. Kang, and R. Ding, 2017a: Western tropical Pacific multidecadal variability forced by the Atlantic multidecadal oscillation. *Nat. Commun.*, **8**, 15998, https://doi.org/10.1038/ncomms15998.

——, J. Li, R. Ding, and Z. Jin, 2017b: Cold season Africa–Asia multidecadal teleconnection pattern and its relation to the Atlantic multidecadal variability. *Climate Dyn.*, **48**, 3903–3918, https://doi.org/10.1007/s00382-016-3309-y.

——, ——, X. Li, J. Xue, R. Ding, F. Xie, and Y. Li, 2018: Oceanic forcing of the interhemispheric SST dipole associated with the Atlantic Multidecadal Oscillation. *Environ. Res. Lett.*, **13**, 074026, https://doi.org/10.1088/1748-9326/aacf66.

——, and Coauthors, 2019: Recent acceleration of Arabian Sea warming induced by the Atlantic-western Pacific trans-basin multidecadal variability. *Geophys. Res. Lett.*, **46**, 1662–1671, https://doi.org/10.1029/2018GL081175.

Takahashi, C., and M. Watanabe, 2016: Pacific trade winds accelerated by aerosol forcing over the past two decades. *Nat. Climate Change*, **6**, 768–772, https://doi.org/10.1038/nclimate2996.

USGCRP, 2018: USGCRP's Indicator Platform (information sheet for March 2018). USGCRP, 2 pp., accessed 23 August 2019, https://www.globalchange.gov/sites/globalchange/files/USGCRP%20indicators_March2018-FINAL_Newsletter%20Version_23May18.pdf.

——, 2019: USGCRP Indicators Catalog. Accessed 23 August 2019, https://www.globalchange.gov/browse/indicators/catalog.

von Laven, K., 2020: GridSphere. MATLAB Central File Exchange, accessed 7 April 2020, https://www.mathworks.com/matlabcentral/fileexchange/28842-grid-sphere.

Wallace, J. M., and D. S. Gutzler, 1981: Teleconnections in the geopotential height field during the Northern Hemisphere winter. *Mon. Wea. Rev.*, **109**, 784–812, https://doi.org/10.1175/1520-0493(1981)109<0784:TITGHF>2.0.CO;2.

Wiens, J. J., 2016: Climate-related local extinctions are already widespread among plant and animal species. *PLOS Biol.*, **14**, e2001104, https://doi.org/10.1371/journal.pbio.2001104.

Wilks, D. S., 2016: "The stippling shows statistically significant grid points": How research results are routinely overstated and overinterpreted, and what to do about it. *Bull. Amer. Meteor. Soc.*, **97**, 2263–2273, https://doi.org/10.1175/BAMS-D-15-00267.1.

Williams, M., and S. Eggleston, 2017: Using indicators to explain our changing climate to policymakers and the public. *WMO Bull.*, **66**, https://public.wmo.int/en/resources/bulletin/using-indicators-explain-our-changing-climate-policymakers-and-public.

Williamson, C. J., and Coauthors, 2019: A large source of cloud condensation nuclei from new particle formation in the tropics. *Nature*, **574**, 399–403, https://doi.org/10.1038/s41586-019-1638-9.

Zhou, C., M. D. Zelinka, and S. A. Klein, 2016: Impact of decadal cloud variations on the Earth's energy budget. *Nat. Geosci.*, **9**, 871–874, https://doi.org/10.1038/ngeo2828.